APPLIED PHYSICS

Chiral electroluminescence from thin-film perovskite metacavities

Seongheon Kim[1], Soo-Chan An[1], Younggon Kim[1], Yun Seop Shin[2], Alexander A. Antonov[3], In Cheol Seo[1], Byung Hoon Woo[1], Yeonsoo Lim[1], Maxim V. Gorkunov[3,4]*, Yuri S. Kivshar[5]*, Jin Young Kim[2,6]*, Young Chul Jun[1,7]*

Chiral light sources realized in ultracompact device platforms are highly desirable for various applications. Among active media used for thin-film emission devices, lead-halide perovskites have been extensively studied for photoluminescence due to their exceptional properties. However, up to date, there have been no demonstrations of chiral electroluminescence with a substantial degree of circular polarization (DCP) based on perovskite materials, being critical for the development of practical devices. Here, we propose a concept of chiral light sources based on a thin-film perovskite metacavity and experimentally demonstrate chiral electroluminescence with a peak DCP approaching 0.38. We design a metacavity created by a metal and a dielectric metasurface supporting photonic eigenstates with a close-to-maximum chiral response. Chiral cavity modes facilitate asymmetric electroluminescence of pairs of left and right circularly polarized waves propagating in the opposite oblique directions. The proposed ultracompact light sources are especially advantageous for many applications requiring chiral light beams of both helicities.

INTRODUCTION

Chirality—nonequivalence to mirror images—is optically manifested by different responses to left circularly polarized (LCP) and right circularly polarized (RCP) light (*1*–*3*). The basic chiral phenomena exhibited by natural materials are circular dichroism and polarization rotation which are both typically very weak. To overcome these limitations, various nanostructures, including three-dimensional chiral structures (e.g., plasmonic helices) and two-dimensional planar chiral structures (e.g., gammadions), have been extensively studied (*4*–*7*). Strongly enhanced chiral light-matter interactions in these nanostructures can be used for important applications (*8*–*13*). Particularly, ultracompact chiral light sources with a large degree of circular polarization (DCP) are highly desirable for displays, optical recording, optical communication, bioimaging, and biomedical diagnosis (*14*–*19*). Although there have been extensive studies on chiral light sources, most studies were limited to special types of chiral molecular materials or photoluminescence (PL).

Thin-film light-emitting diodes (LEDs) have emerged as a key technology for compact light sources (*20*–*22*). Among thin-film LED materials, lead halide perovskites have demonstrated remarkable properties, such as high PL quantum yields, narrow emission width (or high color purity), and high charge-carrier mobility (*23*–*26*). In addition, widely tunable bandgap energy makes perovskite materials ideal for light sources in the visible spectral range. Recently, chiral light sources based on perovskite materials have attracted considerable attention to fully exploit their exceptional material properties. Extensive research has been conducted to obtain chiral PL from perovskite materials (*27*–*35*). For example, chiral perovskite materials can be created by incorporating chiral organic ligands on the surface of perovskite crystals or intercalating chiral organic cations into the perovskite lattice (*27*–*29*). However, achieving large DCP in such chiral perovskite materials at room temperature remains challenging. Chiral electroluminescence (EL) with a large DCP, critical for compact device implementations, has not been demonstrated yet for perovskite materials. There have been chiral EL studies based on chiral organic materials (*36*). Recently, chiral EL was also demonstrated in an organic microcavity using the photonic spin-orbit interaction in a birefringent organic single crystal (*37*). However, there have been no demonstrations of chiral EL with a substantial DCP based on perovskite materials.

Here, we propose, design, fabricate, and demonstrate experimentally a thin-film perovskite ($CsPbBr_3$) metacavity with a peak DCP of chiral EL approaching 0.38 at room temperature, i.e., substantially larger than previously reported cases (*38*–*40*). Our design uses a layer of achiral perovskite confined between metal and a metasurface created by an array of triangular silicon particles with broken inversion symmetry. Chiral Fabry–Pérot modes supported by the metacavity determine the asymmetry of EL, and pairs of LCP and RCP waves of equal powers are generated in the opposite oblique directions. Our theoretical analysis and modeling reveal a crucial role of close-to-maximum chiral metamirror eigenstates underpinning EL chirality. Our approach is based on optical mode properties in the metacavity with symmetry-broken patterns. Therefore, by optimizing the pattern geometry and dimension, we can enhance and tailor the chiral emission from the metacavity. In our metacavity design with triangular patterns, RCP and LCP

[1]Department of Materials Science and Engineering, Ulsan National Institute of Science and Technology (UNIST), Ulsan 44919, Republic of Korea. [2]School of Energy and Chemical Engineering, Ulsan National Institute of Science and Technology (UNIST), Ulsan 44919, Republic of Korea. [3]Shubnikov Institute of Crystallography of the Federal Scientific Research Centre "Crystallography and Photonics", Russian Academy of Science, Moscow 119333, Russia. [4]National Research Nuclear University, MEPhI (Moscow Engineering Physics Institute), Moscow 115409, Russia. [5]Nonlinear Physics Centre, Research School of Physics, Australian National University, Canberra, ACT 2601, Australia. [6]Graduate Graduate School of Carbon Neutrality, Ulsan National Institute of Science and Technology (UNIST), Ulsan 44919, Republic of Korea. [7]Graduate School of Semiconductor Materials and Devices Engineering, Ulsan National Institute of Science and Technology (UNIST), Ulsan 44919, Republic of Korea.
*Corresponding author. Email: ycjun@unist.ac.kr (Y.C.J.); jykim@unist.ac.kr (J.Y.K.); gorkunov@crys.ras.ru (M.V.G.); yuri.kivshar@anu.edu.au (Y.S.K.)

emissions are clearly separated into two well-defined directions ($k_x < 0$ and $k_x > 0$). Moreover, our scheme can be applied to numerous other achiral materials and thus has unique merits. Our experimental and theoretical results suggest using such metacavities as ultracompact sources of chiral light.

RESULTS

Concept of thin-film metacavity

The purpose of the metacavity is to enhance EL from an active perovskite emission layer and to produce high chiral asymmetry, i.e., to support the emission of either LCP or RCP waves in oblique directions. As shown in Fig. 1A, the metacavity is created by stacking the perovskite emission layer between a metal mirror and a specifically designed metamirror. We omit the charge transport interlayers in Fig. 1A for clarity. The optical role of the metamirror is twofold: It performs as a semitransparent mirror supporting Fabry–Pérot cavity modes emitting waves of one circular polarization and it suppresses Fabry–Pérot cavity modes of the opposite handedness emitting light of the opposite polarization. The key precondition for such peculiar functionality is the metamirror ability to selectively interact with circularly polarized waves. More specifically, it performs cross-polarized reflections building Fabry–Pérot loops together with the metal mirror which also inverts circular polarization upon reflection. To promote the cavity modes of particular handedness, the reflections by the metamirror are to have chiral asymmetry which is allowed only for oblique directions by the Lorentz reciprocity theorem, regardless of the metamirror type. Moreover, the reciprocity implies that such reflection asymmetry is reversed for the opposite oblique directions. Therefore, a feasible realization of chiral metacavity backed by a metal mirror is bound to emit with high DCP only in certain oblique directions. Emission with lower and eventually zero DCP is to be possibly minimized for the sake of the overall device efficiency.

For a particular realization of the metamirror, we choose a square lattice of triangular polycrystalline silicon (poly-Si) particles; see the inset in Fig. 1A. Recently, various dielectric metasurfaces built as arrays of particles of high-refractive-index materials have repeatedly demonstrated selective interaction with circularly polarized light provided that their eigenstates are adjusted to the so-called maximum chirality (*41*, *42*). For the normal light incidence, this requires nontrivial nonplanar designs with variable height. For

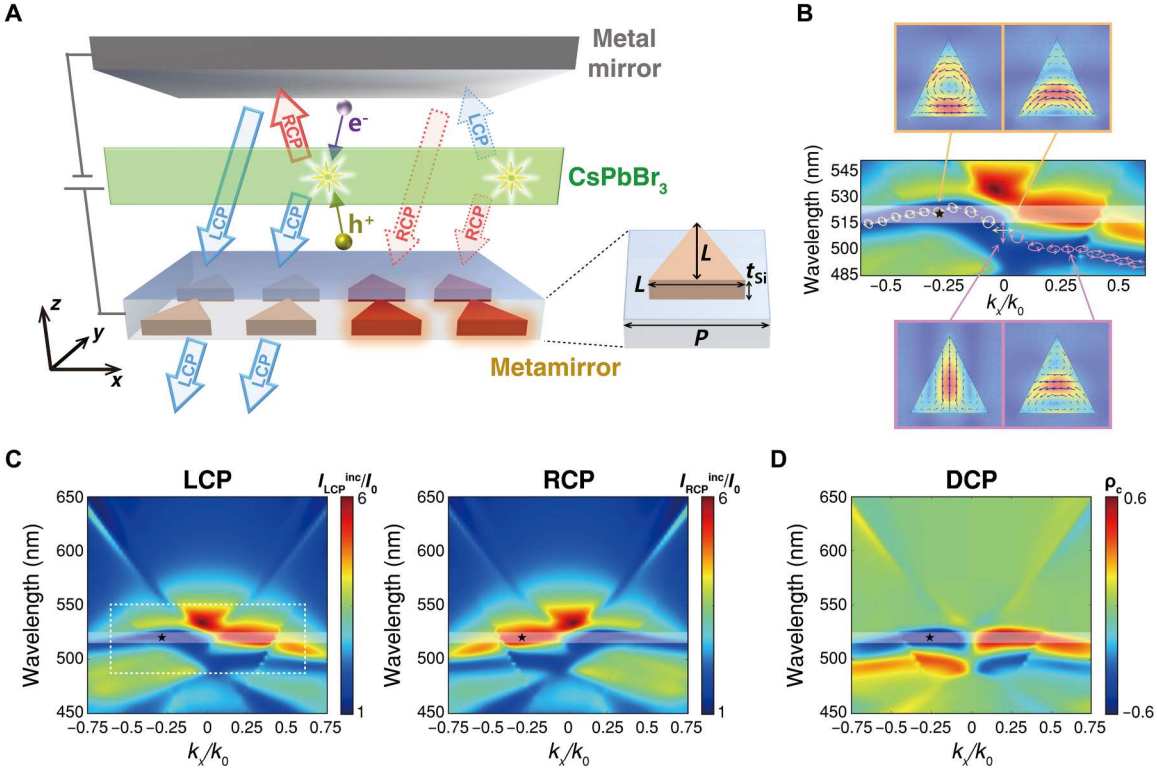

Fig. 1. Concept of thin-film metacavity for chiral EL. (**A**) Schematic of the cavity formed by a metal mirror and a metamirror consisting of inversion symmetry–broken poly-Si patterns immersed in a transparent indium tin oxide (ITO) electrode. Inset: Square unit cell of the pattern containing a poly-Si triangle with the main dimensions indicated. For an oblique direction, the metacavity can support a Fabry–Pérot resonance for the light emission of one circular polarization, while it suppresses the resonance for the other polarization. For the opposite oblique direction, the situation is reversed, and the emission of the opposite circular polarization is obtained. (**B**) Numerically obtained (see Materials and Methods) eigenstate spectra of the poly-Si triangular pattern with polarization ellipses shown on the line, superimposed on the LCP intensity enhancement colormap. Several representative polarization current distributions in the middle cut of a triangle for the linearly polarized (for normal incidence) and close-to-circularly polarized (for oblique incidence) eigenstates are given with the displacement current shown by blue arrows. (**C**) Colormaps of intensity enhancement factor of LCP and RCP light (cavity thickness d = 150 nm) with the fragment shown in (B) indicated by the white dashed frame. (**D**) The corresponding DCP colormap. The simulated data are obtained for the realistic structure including all device layers. The emission band (515 to 525 nm) is indicated by shaded stripes in (B) to (D).

obliquely incident waves, simpler planar structures with broken inversion symmetry can perform in the extrinsic-chiral regime (*43*), and triangular silicon particles nicely fulfill the task. With the dimensions properly adjusted (L = 200 nm, t_{Si} = 40 nm, P = 270 nm), they host photonic eigenstates with a narrowband spectrum crossing the $CsPbBr_3$ emission band (wavelengths, ~520 nm) as shown in Fig. 1B. Apart from the close-to-normal directions, the eigenstate polarization is very close to ideal circular in a wide range of the angles of incidence. This close-to-maximum chiral eigenstate together with the background metasurface reflection contributes to the formation of the metacavity resonance in the extrinsic-chiral regime (see also note S1). For an oblique direction, the metacavity can support a Fabry–Pérot resonance and corresponding field enhancement inside the cavity only for EL of one circular polarization. For the opposite oblique direction, the situation is reversed, and the EL of the opposite circular polarization is obtained. Note that, as discussed above, both metal and metamirrors flip circular polarizations upon reflection, so that the cavity modes of the opposite handedness remain uncoupled. In a more general context, the flipping makes the cavity qualitatively different from those built of pairs of helicity-preserving metamirrors (*44*–*46*).

The DCP of EL is defined by the intensities of emitted circularly polarized waves as $\rho_c = (I_{RCP} - I_{LCP})/(I_{RCP} + I_{LCP})$ and it can be conveniently evaluated according to the reciprocity principle. The power and polarization in the far field of an ensemble of randomly positioned and oriented dipole sources can be obtained by solving the reciprocal problem for the incidence of correspondingly polarized and directed plane waves and by evaluating the field intensity enhancement factors $I^{inc}_{RCP,LCP}/I_0$ as integrals over all dipole positions (see Materials and Methods). Accordingly, we simulate RCP and LCP waves incident onto the metacavity at different angles, integrate the intensity of the electric fields in the perovskite emitting layer, and obtain the enhancement factor for each angle. The colormaps in Fig. 1C show the LCP and RCP intensity enhancement factors (cavity thickness d = 150 nm). The colormaps are given in the axes of free-space light wavelength λ and the in-plane wave vector component k_x/k_0, where $k_0 = 2\pi/\lambda$. The corresponding DCP colormap is also shown in Fig. 1D. The shaded regions on all colormaps represent the $CsPbBr_3$ emission band near a 520-nm wavelength and they nicely cover the range of the strongest EL chirality (maximum DCP). Therefore, efficient implementations of the metacavity concept require fine spectral adjustment of the metasurface eigenstates, cavity modes, and the emission band. In the following, we account for the theory behind the main design steps.

Coupled-mode theory of chiral metacavity

Coupled-mode theory phenomenology describes the resonant response of metasurfaces including those with intrinsic optical chirality (*41*, *42*, *46*, *47*). It can be generalized to account for the extrinsic chiral effects as light is obliquely incident upon a metamirror with broken inversion symmetry (see note S2 for details). The corresponding co-polarized reflection and cross-polarized transmission coefficients read as

$$r_{RR} = r_{LL} = t_{RL} = t_{LR} = -\frac{m_R m_L}{i(\omega - \omega_0) - \gamma_0} \tag{1}$$

while the cross-polarized reflection and co-polarized transmission coefficients are

$$r_{RL} = \rho - \frac{m_L^2}{i(\omega - \omega_0) - \gamma_0},\ r_{LR} = \rho - \frac{m_R^2}{i(\omega - \omega_0) - \gamma_0} \tag{2}$$

$$t_{RR} = \tau - \frac{m_R^2}{i(\omega - \omega_0) - \gamma_0},\ t_{LL} = \tau - \frac{m_L^2}{i(\omega - \omega_0) - \gamma_0} \tag{3}$$

where r_{ij} and t_{ij} indicate the reflection and transmission coefficients of the output polarization i from the input polarization j, respectively, and τ and ρ are the background transmission and reflection coefficients, respectively. The resonant terms correspond to the excitation of a photonic eigenstate, ω_0 is its frequency, γ_0 is its decay rate, and $m_{R,L}$ are the parameters of the eigenstate coupling to RCP and LCP waves, respectively. For a known distribution of the eigenstate displacement current density $\mathbf{J}(\mathbf{r})$, the coupling parameters are proportional to the overlap integrals (*41*)

$$m_{R,L} \propto \int_V \mathbf{J}(\mathbf{r}) \cdot \mathbf{e}_{R,L}\, e^{i\mathbf{k}\cdot\mathbf{r}}\, dV \tag{4}$$

where $\mathbf{e}_{R,L}$ is the electric field unit vector of an RCP or LCP wave and $\mathbf{k}$ is its wave vector.

To decouple the state from RCP waves, it is sufficient to set m_R = 0 which establishes the maximum extrinsic chirality. As seen from the diagram in Fig. 1B, the metamirror eigenstate closely approaches this condition in a wide range of the angles of incidence. To quantitatively analyze the underlying mechanism, we apply a multipole

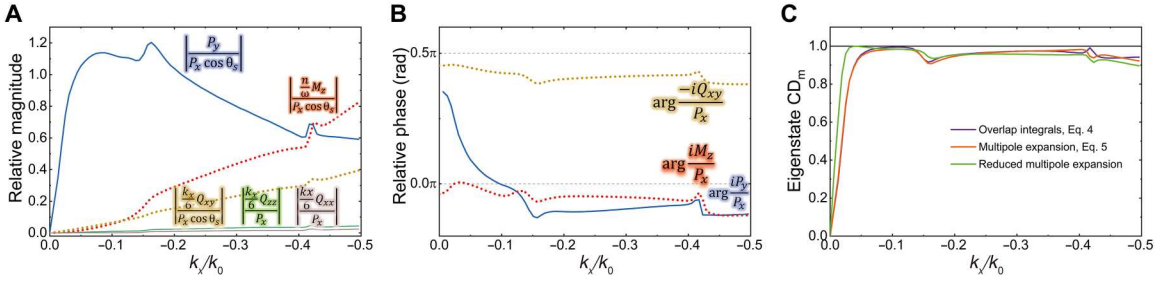

Fig. 2. Multipolar mechanism of metamirror maximum chirality. (**A**) Relative magnitudes of the multipolar terms contributing to the coupling parameters in Eq. 5. (**B**) Relative phases of the three substantial terms as counted from the phase of P_x. (**C**) Comparison of the eigenstate circular dichroism evaluated by the integrals (Eq. 4), using the multipole expansion (Eq. 5), and by the reduced expansion taking into account only the main contributions (equation 3.4 in note S3).

expansion to Eq. 4 and express it as (note S3)

$$m_{R,L} \propto P_x \cos\theta_s \mp iP_y \pm i\frac{k_x}{\omega}M_z - \frac{k_x}{6}[\cos\theta_s(Q_{zz} - Q_{xx}) \pm iQ_{xy}] \quad (5)$$

where P_i, M_i, and Q_{ij} are the Cartesian components of the eigenstate electric dipole, magnetic dipole, and electric quadrupole moments, respectively, and θ_s is the angle of incidence from the glass substrate. Numerically obtaining the eigenstate current distribution $\mathbf{J}(\mathbf{r})$, we evaluate and compare the relative magnitudes and phases of the terms entering Eq. 5 in Fig. 2 (A and B), correspondingly. One can see that the diagonal quadrupole components contribute negligibly, iP_y and iM_z contribute almost exactly in-phase with P_x, while iQ_{xy} contributes with a relative $\pi/2$ phase shift. Therefore, the condition $m_R = 0$ can be approached as a result of the mutual compensation of the first three dipolar terms in Eq. 5.

To quantify the degree of eigenstate coupling selectivity, we introduce the eigenstate circular dichroism defined as

$$\mathrm{CD}_m = \frac{|m_L|^2 - |m_R|^2}{|m_L|^2 + |m_R|^2} \quad (6)$$

Comparing its values obtained using Eqs. 4 and 5, as well as using the reduced multipole expansion accounting only for the main contributions (note S3), we find that the eigenstate closely approaches the maximum extrinsic chirality, as its CD stays close to unity in a very broad range of the angles of incidence (see Fig. 2C). The multipolar content of the state varies with the angle. For smaller angles, the magnetic dipole contribution is almost negligible, and the chirality is provided by the interplay of the electric dipole components P_x and P_y which are shifted by $\pi/2$ in phase. At larger angles, the magnetic dipole moment contributes more substantially, although both components of the electric dipole also play similarly important roles.

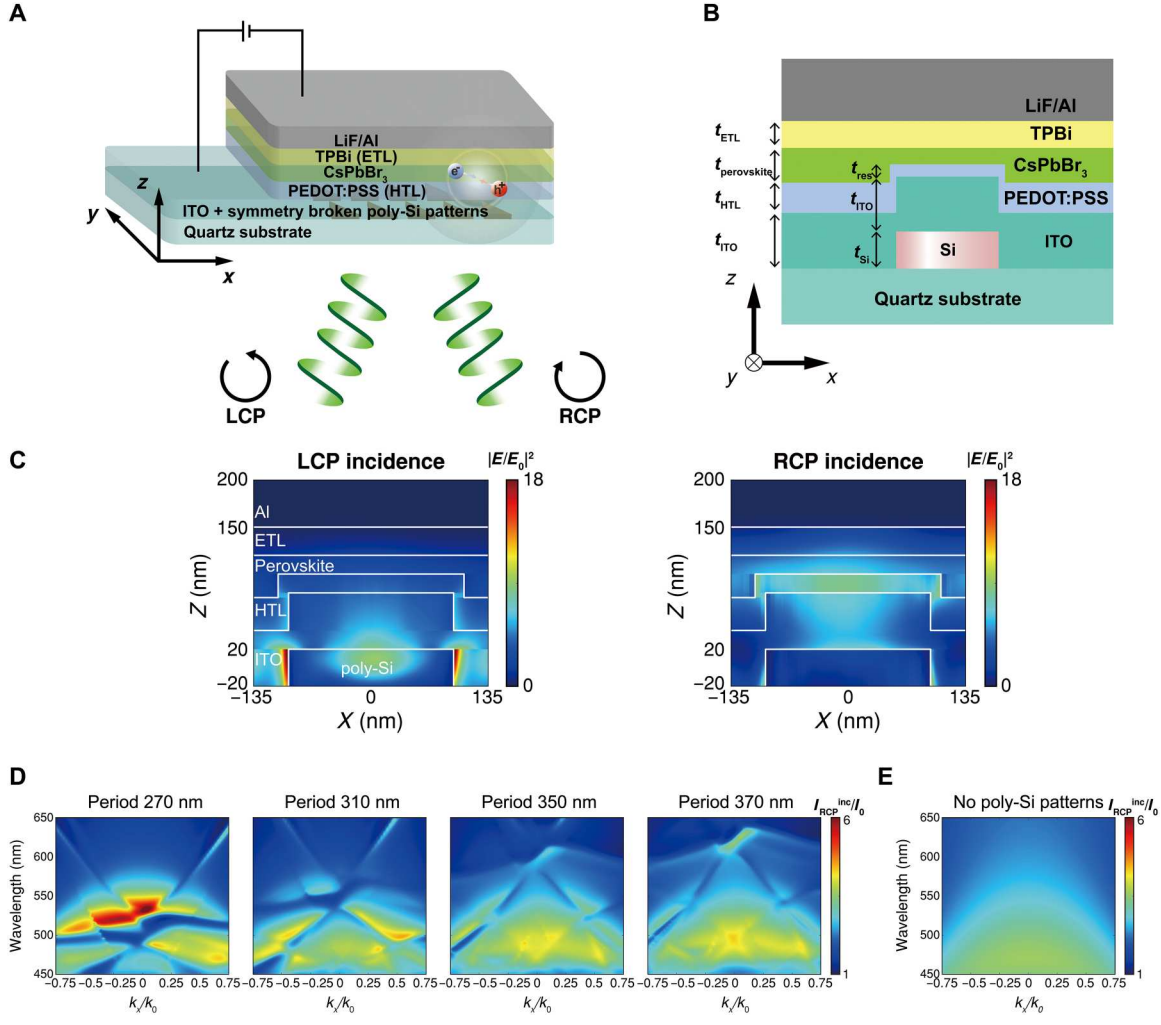

Fig. 3. Sample geometry and numerical simulations. (**A** and **B**) Schematic of the simulation configuration. t_{Si} = 40 nm, t_{ITO} = 60 nm, t_{HTL} = 35 nm, $t_{perovskite}$ = 45 nm, t_{res} = 20 nm, and t_{ETL} = 30 nm. The cavity thickness d is defined as the distance from the metal layer to the top surface of the bottom poly-Si layer. (**C**) Field profiles for the LCP and RCP incidences at the positions marked as stars in Fig. 1C. (**D**) Period scan in the reciprocity calculations of the triangular pattern under RCP incidence (d = 150 nm). (**E**) Reciprocity calculation without poly-Si patterns (i.e., conventional flat thin-film LED geometry). The emission intensity is weaker, and no chiral response is present. PEDOT:PSS, poly(3,4-ethylenedioxythiophene):poly(styrene sulfonate); TPBi, 1,3,5-tris(N-phenylbenzimidazol-2-yl) benzene.

Knowing the metamirror characteristics, one can obtain analytical expressions for the fields inside the metacavity and evaluate the intensity enhancement factors. As both the metamirror and the metal mirror reflect LCP/RCP light flipping its helicity and the metamirror transmits preserving the helicity, the cavity modes of opposite handedness remain uncoupled. The LCP and RCP enhancement factors are obtained from two independent problems (note S2) as proportional to

$$\frac{I_{\mathrm{LCP}}^{\mathrm{inc}}}{I_0} \propto \frac{|t_{LL}|^2}{|1 - r_{RL} r_{\mathrm{metal}}\, e^{2ik_z d}|^2}, \frac{I_{\mathrm{RCP}}^{\mathrm{inc}}}{I_0} \propto \frac{|t_{RR}|^2}{|1 - r_{LR} r_{\mathrm{metal}}\, e^{2ik_z d}|^2} \quad (7)$$

where r_{metal} is the reflection coefficient of the metal mirror and k_z is the vertical wave vector component. One can readily use Eq. 7 to explain the chiral asymmetry of field enhancement and, correspondingly, high DCP of EL. For example, for the exemplary wavelength and direction indicated by the black star in Fig. 1 (B to D), the transmission and reflection coefficients are given in fig. S8, where $|t_{LL}|$ has a resonance dip around 520 nm (therefore, $|t_{RR}| > |t_{LL}|$). In addition, the phases of r_{RL} and r_{LR} are substantially different, and thus, the denominator in Eq. 7 also contributes to the field intensity and DCP. In general, depending on the cavity thickness d, a very different type of interplay between the resonant reflection (determined by m_L and m_R) and the broad background reflection (determined by ρ) from the metamirror appears (see figs. S2C and S3). This metacavity response can be used to optimize the emission intensity and DCP of chiral EL.

Sample geometry and numerical simulations

Now, we explain the EL device structure including all device layers. Because of the bottom poly-Si layer, the device layer is not planar. The device layer geometry was determined from atomic force microscopy (AFM) measurements. After spin-coating of each layer, a height profile was measured using AFM (fig. S12). Figure 3 (A and B) shows the device geometry we used in simulations (layer thickness and shape). We used this geometry in the numerical simulations of the realistic device structure. The complex refractive indices used in simulations (at 520 nm) are as follows: n(Al) = 0.83 + 6.26i, n(TPBi) = 1.75, n($CsPbBr_3$) = 1.96 + 0.035i, n(PEDOT:PSS) = 1.5, n(ITO) = 1.89 + 0.004i, n(poly-Si) = 4.11 + 0.085i. The complex refractive indices of $CsPbBr_3$, indium tin oxide (ITO), and poly-Si were measured using ellipsometry. The refractive indices of the organic layers and aluminum were obtained from (*22*) and from the *Handbook of Optical Constants of Solids* (by Palik) (*48*), respectively.

Figure 3C shows the field profiles for LCP and RCP incidences at the positions indicated in Fig. 1C as stars. The field profiles in the emitter layer show a clear difference between the LCP and RCP incidences, which leads to chiral emission via reciprocity. Figure 3D shows the period scan in the reciprocity calculations. The emission enhancement factor was obtained by integrating the field intensities in the perovskite emitter layer under CP plane wave incidence (see Materials and Methods). Here, we vary the period while keeping the fill fraction of the triangular pattern constant. The cavity thickness was fixed as d = 150 nm. In this way, the spectral position of the background Fabry–Pérot resonance remains almost the same, whereas the narrow mode dispersion gradually shifts upward with the increasing pattern period. The spectral overlap of the background and narrow mode resonances is achieved at a period of 270 nm. We find that chiral emission with a large DCP can be achieved near 520 nm. We also identify that the top metal layer in our design plays an important dual role; it works as an electrode for carrier injection and also as a cavity mirror that strongly confines the optical fields inside the cavity.

Sample fabrication and reflectance measurements

In our EL device, a square lattice of poly-Si patterns is integrated with a perovskite EL device. Perovskite EL was measured on the transparent substrate side (Fig. 3A). First, arrays of poly-Si patterns were created on a fused quartz substrate using electron-beam lithography. Each array has a different pattern shape (triangle or circle) and lattice period. Figure S13 shows the optical microscopy and

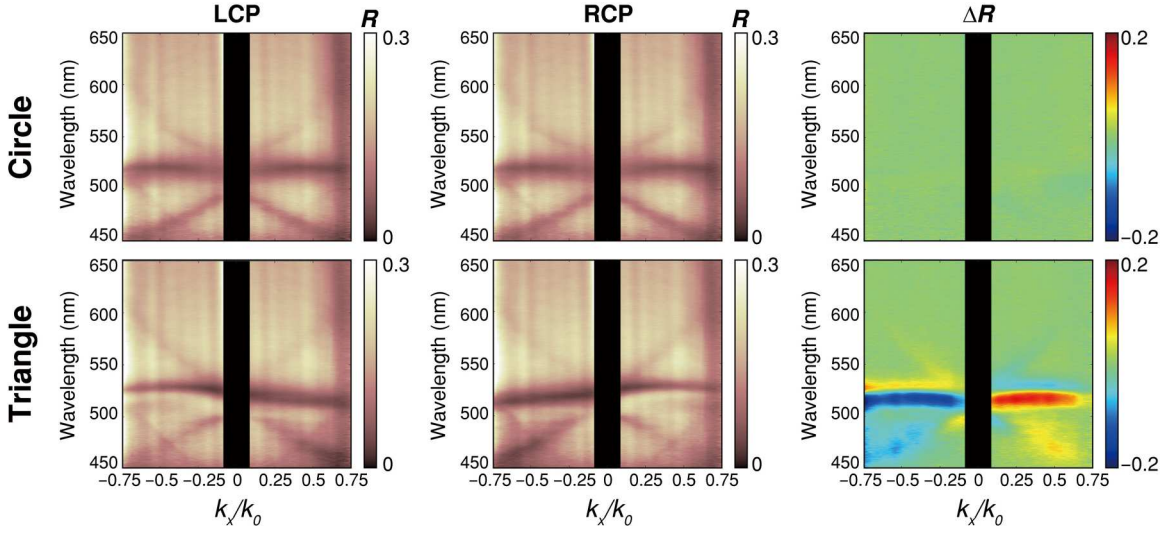

Fig. 4. Reflectance measurements and chiral optical response. Experimentally measured reflectance spectrum map as a function of in-plane wave vector and wavelength under LCP and RCP incidences (for the 270-nm period). The top and bottom rows compare the reflectance from the cavity with the circular and triangular patterns, respectively. The triangular pattern shows a clear chiral response.

scanning electron microscopy images of the poly-Si patterns. On top of the poly-Si patterns, a 60-nm-thick ITO layer was first deposited. Then, a hole transport layer and an inorganic polycrystalline perovskite emitter layer ($CsPbBr_3$) were spin-coated in succession (*49*, *50*). Last, an electron transport layer and metal contact (LiF/Al) were sequentially deposited using a thermal evaporator. The measured cavity thickness was $d \sim 150$ nm. The top metal contact has a circular shape with a 2-mm diameter and includes arrays of poly-Si patterns underneath. Figure S14A shows the PL and EL spectra from a reference sample without poly-Si patterns; $CsPbBr_3$ has an emission peak near 520 nm with a full width at half maximum of 18 nm. The narrow emission width of perovskite materials can be advantageous because of the limited spectral bandwidth in chiral responses. Figure S14B shows the absorbance spectrum of a bare $CsPbBr_3$ film spin-coated on a quartz substrate, and fig. S14C presents the refractive index of the poly-Si film measured using ellipsometry.

To experimentally characterize the chiral response of our device, we first measured the angle-resolved reflectance spectrum using a custom-built Fourier-plane (or momentum-space) measurement setup. CP light was incident from the substrate side, and the total reflection intensity was measured. The top and bottom rows in Fig. 4 compare the reflectance from the cavity with the circular and triangular patterns, respectively. The triangular pattern shows a clear chiral response. The central region near $k_x = 0$ in the reflectance map is intentionally shaded in a dark color to block the direct intense reflection from the top metal layer. The reflectance map shows a resonance dip (dark line) at the cavity resonance position on top of a bright background owing to the reflection from the top metal surface. Each spectrum map exhibits the dispersion of the cavity resonances in the device, excited by LCP or RCP incident light. In the case of the circular pattern, the LCP and RCP reflectance spectra show the same behavior along the k_x direction. However, in the case of the triangular pattern, a clear chiral response appears; the LCP and RCP reflectance maps show distinctly different mode dispersions near the emission band (~520 nm). It also compares the differential reflectance ΔR ($= R_{RCP} - R_{LCP}$) of the circular and triangular patterns. The cavity with the triangular pattern exhibits a clear chiral response, and we note that the sign of ΔR is opposite for positive and negative incidence angles. Using momentum-space tomography, we also constructed the cavity mode dispersion in the entire energy-momentum space [within the numerical aperture (NA) of a microscope objective] and further confirmed the chiral response of the metacavity resonances (fig. S16).

Measurements of EL and PL

To characterize the emission properties of our device, we measured EL and PL spectra in the Fourier plane. The chiral responses of the thin-film cavities with the triangular and circular patterns were compared. The LCP and RCP emission spectra were measured using a quarter–wave plate and a linear polarizer. Because the circular metal contact (diameter, 2 mm) includes arrays of the poly-Si patterns underneath, a pinhole was placed in the real-space plane for the EL measurements to collect emission from the patterned region only (60 μm by 60 μm in size for each array) (fig. S13A). The emission spectrum was then measured in the Fourier plane.

We directly compare EL and PL spectra to characterize the emission properties of our device. Figure 5 presents the EL and PL DCP maps as a function of λ and k_x/k_0. Because the DCP is the ratio of the RCP and LCP emission intensities, the DCP map becomes noisy outside of the emission band owing to small emission intensities. The upper row in Fig. 5A shows the EL DCP maps from the triangular pattern for the periods of 250, 260, and 270 nm, respectively (fig. S18 shows the separate RCP and LCP emission spectra for the 270-nm period). EL from the triangular pattern shows clear chiral responses, which agrees with our reciprocity calculations in Fig. 1D. The chiral emission band gradually redshifts with the increase in the pattern period. The PL spectrum (the lower row in Fig. 5A) also shows the same behavior. Figure 5 (C and D) shows the EL line spectra and the corresponding DCP at $k_x/k_0 = -0.27$ and $k_x/k_0 = +0.27$ (period 270 nm), respectively. The EL spectrum shows a clear chiral response; the LCP EL intensity is larger for $k_x < 0$, while the RCP EL intensity is larger for $k_x > 0$. The peak DCP reaches $\rho_c \approx 0.38$, which is the largest EL DCP in perovskite materials to our knowledge. In contrast, EL and PL from the circular pattern (diameter: 150 nm) do not show such a chiral response along the k_x direction (Fig. 5B).

We also conducted emission measurements over the k_x-k_y plane (or Fourier plane) and obtained EL and PL images. Each point in the k_x-k_y plane corresponds to a different far-field emission angle. Therefore, the EL and PL images in the Fourier plane indicate the far-field emission pattern from our device. Figure 6A presents a comparison of the LCP and RCP components for the EL (top row) and PL (bottom row) from the thin-film metacavity with the triangular pattern. The EL and PL images were measured using a 10-nm bandpass filter at 520 nm. In both EL and PL images, the LCP and RCP emissions are stronger for the negative k_x and positive k_x regions, respectively. This means that LCP and RCP waves are emitted into the opposite oblique directions, as dictated by the metasurface *yz* mirror symmetry plane. The angular plot of EL along the k_x direction ($k_y = 0$) confirms this behavior (Fig. 6B). Its comparison with the results of reciprocity-based simulations also provided in Fig. 6B shows good agreement. Figure 6A also shows the corresponding DCP of the EL and PL. The DCP ρ_c in the k_x-k_y plane exhibits clear chiral responses in both cases and is in overall good agreement with the results of reciprocity-based simulations shown in fig. S6. All these emission measurements agree with the cavity mode properties determined from the momentum-space tomography (reflectance) measurements (fig. S16).

We also note that the dark emission line (or suppressed emission) in EL and PL images appears on the opposite side of the bright (or enhanced) emission along the k_x direction (Fig. 6A), which increases the contrast between the LCP and RCP emissions. Because DCP is the ratio of the LCP and RCP emission intensities, DCP in our device is further enhanced by this suppressed emission. The observed suppressed emission agrees well with the reciprocity-based calculations.

We also evaluated the overall efficiency of chiral EL in our experiment. The overall efficiency of chiral EL was defined using the solid angle integration of the emission intensities as follows

$$\eta = \frac{\iint |I_{RCP} - I_{LCP}| \sin\theta d\theta d\varphi}{\iint (I_{RCP} + I_{LCP}) \sin\theta d\theta d\varphi} \quad (8)$$

where I_{RCP} and I_{LCP} are the RCP and LCP EL intensities measured in the k_x-k_y plane. Here, $k_x/k_0 = \sin\theta\cos\varphi$ and $k_y/k_0 = \sin\theta\sin\varphi$. Note that EL data in the k_x-k_y plane were measured using a 10-nm bandpass filter at 520 nm. Therefore, the measured EL and DCP values

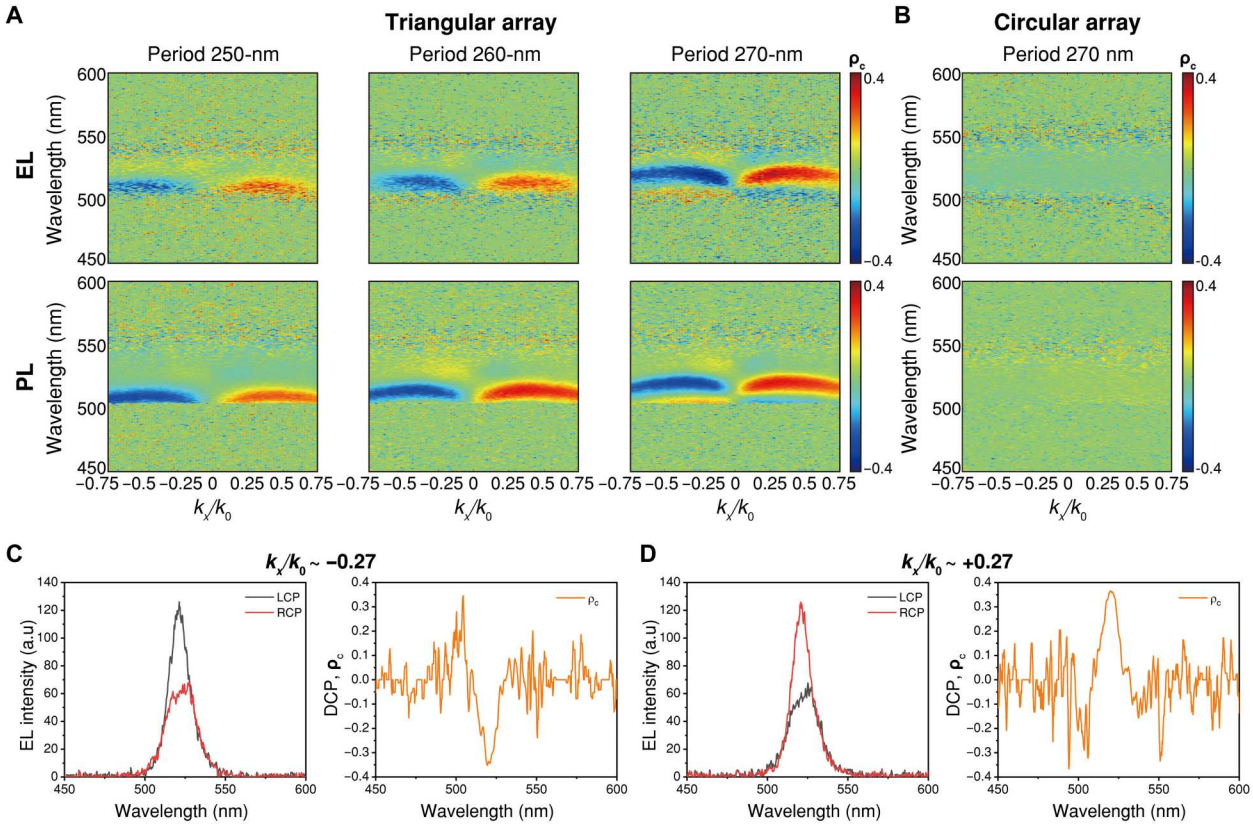

Fig. 5. Experimentally measured EL and PL. (**A**) EL and PL DCP for the triangular pattern of the different pattern periods (250 to 270 nm). The emission DCP is defined as the ratio between the RCP and LCP emission intensities (I_{RCP} and I_{LCP}, respectively): $\rho_c = (I_{RCP} - I_{LCP})/(I_{RCP} + I_{LCP})$. Both EL and PL spectra show similar behavior. (**B**) EL and PL DCP for the circular pattern (period, 270 nm). DCP is close to zero along the k_x direction. (**C** and **D**) EL line spectra and the corresponding DCP at $k_x/k_0 = -0.27$ (or $\theta = -15.7°$) and $k_x/k_0 = +0.27$ (or $\theta = +15.7°$), respectively. The peak EL DCP reaches ~0.38. The spectral width of the chiral response is wide enough to cover a large portion of the emission band. a.u., arbitrary units.

were spectrally averaged over the 10-nm bandwidth. Then, we obtain that the overall efficiency over the whole k_x-k_y plane (within the NA of our microscope objective, NA = 0.75) is η = 9.6%. If we calculate the efficiency along the k_x direction, then we obtain η = 17.35%. This is smaller than the peak DCP value in Fig. 5, but it is still substantially larger than the previous EL DCP values in perovskite materials (*36*–*38*). Our experimental and theoretical studies demonstrate that Fabry-Pérot cavities with tailored mirror responses can be exploited in a clever way to improve the characteristics of the chiral light sources.

DISCUSSION

Our approach is generally applicable to other thin-film LEDs with different emissive materials such as quantum dots (*20*). In our concept and its realization, chiral EL with a substantial value of DCP is achieved from achiral emitters without using spin injection or filters (*38*, *40*). We have experimentally confirmed that both EL and PL spectra show the same types of chiral response being determined by the chiral behavior of the metacavity resonance.

We have clarified theoretically that nearly maximum chirality of the inversion symmetry–broken metamirror results from the interplay of the three dipole moments: two electric dipoles (P_x and P_y) and one magnetic dipole (M_z). In addition, we have explained the physical mechanism of the chirality asymmetry and the field enhancement in thin-film metacavities, thus providing the general strategies for the design of compact EL devices that can enhance simultaneously chiral emission intensity and DCP.

Thus, we have proposed and demonstrated experimentally a new type of light source that exhibits chiral EL in a thin-film device platform. Many chiral applications require both LCP and RCP light of the same power (e.g., circular dichroism and enantiomer selection), and thus, our studies provide novel opportunities for innovative device integration and applications requiring ultracompact sources of chiral light.

MATERIALS AND METHODS

Materials and perovskite synthesis

Cesium bromide (CsBr; 99.999%) and dimethyl sulfoxide (DMSO; 99.9%) were purchased from Sigma-Aldrich. Lead bromide ($PbBr_2$; for perovskite precursors) was purchased from Tokyo Chemical Industry Co. Ltd., and 1,3,5-tris(*N*-phenylbenzimidazol-2-yl) benzene (TPBi; 99.9%) was purchased from OSM. All the chemical materials were used as received without further purification. The precursor solution (0.2 M) for the $CsPbBr_3$ perovskite film was prepared by dissolving CsBr and $PbBr_2$ (molar ratio, 1.7:1.0) in anhydrous DMSO under continuous stirring overnight at 60°C. The perovskite

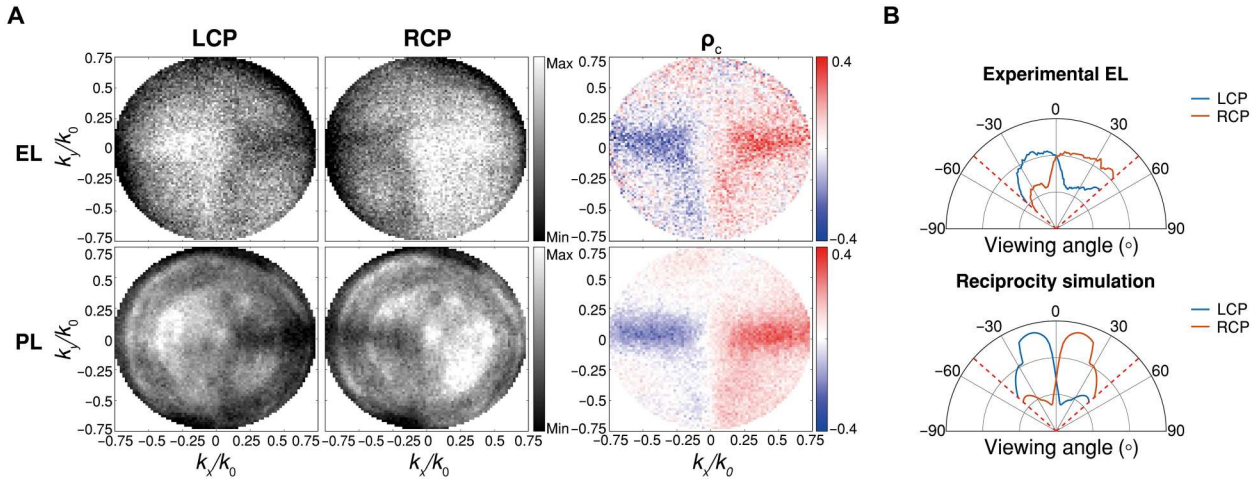

Fig. 6. Fourier-plane images of EL and PL. (**A**) The LCP and RCP emissions are measured in the k_x-k_y plane using a 10-nm bandpass filter at 520 nm (near the peak emission wavelength). The EL and PL DCP (ρ_c) show a strong chiral response along the k_x direction; LCP and RCP emissions are generated into opposite angles. (**B**) Angular distribution of the LCP and RCP emissions along the k_x direction ($k_y = 0$). Top: Experimentally measured EL. Bottom: Reciprocity calculations (averaged in the wavelength range of 515 to 525 nm). The orange dotted lines indicate the detection limit due to the numerical aperture of a microscope objective (corresponding to 48.6°).

precursor solution was filtered with a pore size of 0.20 μm before use. The polycrystalline perovskite films were obtained by spin-coating at 4000 rpm for 60 s and the resulting films were annealed at 100°C for 10 min.

Fabrication of poly-Si patterns

A poly-Si film (thickness, 40 nm) was deposited on a fused (amorphous) quartz substrate using low-pressure chemical vapor deposition at 565°C, followed by annealing for 1 hour at 950°C. Arrays of triangular and circular patterns were created in the poly-Si film using electron-beam lithography and dry etching. The side length L of the triangular pattern is 200 nm, while the diameter of the circular pattern is 150 nm. The lattice period is varied from 250 to 270 nm. The patterned arrays were first created on a polymethyl methacrylate resist (AR-P 6200.09). The size of each array was 60 μm by 60 μm. After developing the patterned resist, a Cr thin film was deposited as a hard mask for dry etching using an electron beam evaporator, followed by a liftoff process. The inductively coupled plasma reactive ion etching was then conducted using an Ar and Cl_2 gas mixture as the main etchant to create patterns in the poly-Si film. Last, the Cr hard mask was removed using a Cr etchant purchased from Sigma-Aldrich.

EL device fabrication

To fabricate an EL device, a 60-nm-thick ITO film was first deposited on the patterned poly-Si structure. The sample was then sequentially cleaned by ultrasonication in deionized water, acetone, and isopropyl alcohol and dried in an oven overnight at 80°C. The substrate was then treated with ultraviolet ozone for 30 min before spin-coating of poly(3,4-ethylenedioxythiophene):poly(styrene sulfonate) (PEDOT:PSS). The PEDOT:PSS solution was spin-coated at 3000 rpm for 40 s, and then annealed at 140°C for 15 min. After spin-coating of the $CsPbBr_3$ film, TPBi (30 nm), LiF (1 nm), and Al (100 nm) was sequentially deposited by thermal evaporation under high vacuum (<10^{-6} Torr). The thickness and structural profile of each layer were determined using AFM (fig. S12).

Reflectance measurement and momentum-space tomography

The dispersion of the cavity modes in our device was measured in a custom-built Fourier-plane setup. To conduct angle-resolved reflectance measurements, the back focal plane of the microscope objective was imaged instead of the device sample surface. The spectrum in the Fourier plane was measured using a monochromator slit as the line aperture in the Fourier plane (see the setup schematic in fig. S15). Both reflectance and luminescence measurements were performed from the quartz side. The in-plane wave vector k_x is defined as $k_x = k_0 \sin\theta$, where θ is the incidence angle along the x axis. Note that refraction occurs at the quartz/air interface; thus, the internal and external angles are different in our case. Throughout this study, we used the external angles measured in air.

The chiral responses of the cavity modes were characterized using reflectance measurements. Collimated white light was circularly polarized using a broadband Glan Thompson linear polarizer and quarter–wave plate and focused on the sample surface using a high NA microscope objective (NA = 0.75). The total intensity of the reflected beam was then measured. The measured raw reflectance spectrum was normalized to the background reflectance of a flat silver film. For momentum-space tomography, the lens in front of the monochromator slit was gradually moved using a motorized microstage to construct the reflectance map in energy-momentum space.

Measurements of luminescence spectra

Angle-resolved luminescence spectrum measurements were also conducted using the Fourier-plane setup. The PL spectrum of the device was measured using a linearly polarized diode laser at 450 nm as an excitation light source. The circular polarization of PL and EL was measured using a linear polarizer and quarter–wave plate. All measurements were conducted at room temperature. For the EL measurements, the bottom ITO film was used as an anode and biased against the circular top metal contact. A continuous bias (4 to 4.5 V) was applied to measure EL. The EL from each pattern array (60 μm by 60 μm in size) was extracted using real-space

filtering for spectral measurements. The emission DCP ρ_c is defined as the ratio between the RCP and LCP emission intensities (I_{RCP} and I_{LCP}, respectively): $\rho_c = (I_{RCP} - I_{LCP})/(I_{RCP} + I_{LCP})$. It is also related to the normalized Stokes parameter: $\rho_c = S_3/S_0$.

To obtain the Fourier-plane images of EL and PL (Fig. 6), the monochromator slit was fully opened, and the monochromator grating was set to the zero position. The Fourier plane was directly imaged on a two-dimensional charge-coupled device camera. The far-field emission profile of the device can be measured in the Fourier (k_x-k_y) plane. The radius of the Fourier-plane image corresponds to the NA of the microscope objective. The EL and PL images were measured using a 10-nm bandpass filter at 520 nm. The bandpass filter covered the emission band near the peak emission wavelength.

Reciprocity calculation of circularly polarized emission

The reciprocity principle states that the source and detector of electromagnetic fields can be interchanged without affecting the physical situation (*51*). Therefore, the far-field radiation power and polarization from an ensemble of randomly positioned and oriented dipolar emitters can be obtained by simply calculating the field enhancements at the dipole positions under incident light (*52*, *53*). The reciprocity principle ensures that the field enhancement calculation in the emission layer produces the same result as the dipole simulation. However, compared to typical dipole simulations, the reciprocity calculation simplifies emission simulations and also enables a deeper understanding of the emission process in our device because the field enhancement in a photonic cavity is more straightforward to understand and optimize.

The reciprocity principle states that, for any two current densities $\mathbf{j}_{1,2}$,

$$\int \mathbf{j}_1 \cdot \mathbf{E}_2 dV = \int \mathbf{j}_2 \cdot \mathbf{E}_1 dV \tag{9}$$

where $\mathbf{E}_{1,2}$ is the electric fields produced by $\mathbf{j}_{1,2}$. For a dipole source $\mathbf{p}_m$, where $\mathbf{j}_m = -i\omega \mathbf{p}_m \delta(\mathbf{r} - \mathbf{r}_m)$ ($m = 1, 2$), this is simplified to

$$\mathbf{p}_1 \cdot \mathbf{E}_2(\mathbf{r}_1) = \mathbf{p}_2 \cdot \mathbf{E}_1(\mathbf{r}_2) \tag{10}$$

The DCP is then determined by the intensity enhancement factors $I^{inc}_{RCP,LCP}/I_0$ integrated across the perovskite emitting layer obtained by solving the reciprocal problem of illumination by reversely propagating incoming plane waves. For circular polarizations, the reciprocal problem with interchanged sources and detectors involves waves of the same helicity (*47*), but, additionally, interchanging obliquely incident and emitted waves implies reversing the in-plane wave vector component. In the considered geometry, this is equivalent to the handedness inversion, and, for simplicity, we preserve the in-plane wave vector component and evaluate DCP as $\rho_c = (I^{inc}_{LCP} - I^{inc}_{RCP})/(I^{inc}_{LCP} + I^{inc}_{RCP})$.

Metamirror eigenstate analysis

The complex eigenfrequencies and polarization current distributions of the metasurface eigenstates are numerically obtained using the COMSOL Multiphysics eigenvalue solver. The corresponding overlap integrals (Eq. 4) and the multipole moments entering Eq. 5 are numerically evaluated. To analyze the eigenstate polarization, we calculate the integrals $m_\alpha = \int J_\alpha(\boldsymbol{r}) e^{i\mathbf{k}\cdot\mathbf{r}}\, dV$, $\alpha = x$, y, z, then extract the components of vector $\mathbf{m}$ orthogonal to $\mathbf{k}$ and consider them in the reference frame of obliquely incident wave as components of a Jones vector. The eigenstate coupling to RCP/LCP waves is described by $m_{R,L} = \mathbf{m}\cdot\mathbf{e}_{R,L}$, where $\mathbf{e}_{R,L} = (\mathbf{e}_{x'} \mp i\mathbf{e}_y)/\sqrt{2}$ is defined in the oblique Cartesian coordinate system (x', y, z') with the z' axis directed along $\mathbf{k}$. To visualize the eigenstate polarization in Fig. 1B, we use ellipses as symbols and their shape and inclination characterize the eigenstate polarization in a conventional way, while their size is inversely proportional to the eigenstate quality factor.

Supplementary Materials

This PDF file includes:

Notes S1 to S3
Figs. S1 to S20
References

REFERENCES AND NOTES

1. S. Boriskina, N. Zheludev, *Singular and Chiral Nanoplasmonics* (Jenny Stanford Publishing, 2014).
2. M. Hentschel, M. Schäferling, X. Duan, H. Giessen, N. Liu, Chiral plasmonics. *Sci. Adv.* **3**, e1602735 (2017). 10.1126/sciadv.1602735.
3. Y. Chen, W. Du, Q. Zhang, O. Ávalos-Ovando, J. Wu, Q.-H. Xu, N. Liu, H. Okamoto, A. O. Govorov, Q. Xiong, C.-W. Qiu, Multidimensional nanoscopic chiroptics. *Nat. Rev. Phys.* **4**, 113–124 (2022). 10.1038/s42254-021-00391-6.
4. J. K. Gansel, M. Thiel, M. S. Rill, M. Decker, K. Bade, V. Saile, G. von Freymann, S. Linden, M. Wegener, Gold helix photonic metamaterial as broadband circular polarizer. *Science* **325**, 1513–1515 (2009). 10.1126/science.1177031.
5. E. Hendry, T. Carpy, J. Johnston, M. Popland, R. V. Mikhaylovskiy, A. J. Lapthorn, S. M. Kelly, L. D. Barron, N. Gadegaard, M. Kadodwala, Ultrasensitive detection and characterization of biomolecules using superchiral fields. *Nat. Nanotechnol.* **5**, 783–787 (2010). 10.1038/nnano.2010.209.
6. S. Zhang, J. Zhou, Y.-S. Park, J. Rho, R. Singh, S. Nam, A. K. Azad, H.-T. Chen, X. Yin, A. J. Taylor, X. Zhang, Photoinduced handedness switching in terahertz chiral metamolecules. *Nat. Commun.* **3**, 942 (2012). 10.1038/ncomms1908.
7. X. Yin, M. Schäferling, B. Metzger, H. Giessen, Interpreting chiral nanophotonic spectra: The plasmonic Born–Kuhn model. *Nano Lett.* **13**, 6238–6243 (2013). 10.1021/nl403705k.
8. K. Konishi, M. Nomura, N. Kumagai, S. Iwamoto, Y. Arakawa, M. Kuwata-Gonokami, Circularly polarized light emission from semiconductor planar chiral nanostructures. *Phys. Rev. Lett.* **106**, 057402 (2011). 10.1103/PhysRevLett.106.057402.
9. X. Zhang, Y. Liu, J. Han, Y. Kivshar, Q. Song, Chiral emission from resonant metasurfaces. *Science* **377**, 1215–1218 (2022). 10.1126/science.abq7870.
10. W. Li, Z. J. Coppens, L. V. Besteiro, W. Wang, A. O. Govorov, J. Valentine, Circularly polarized light detection with hot electrons in chiral plasmonic metamaterials. *Nat. Commun.* **6**, 8379 (2015). 10.1038/ncomms9379.
11. J. Kumar, H. Eraña, E. López-Martínez, N. Claes, V. F. Martín, D. M. Solís, S. Bals, A. L. Cortajarena, J. Castilla, L. M. Liz-Marzán, Detection of amyloid fibrils in Parkinson's disease using plasmonic chirality. *Proc. Natl. Acad. Sci. U.S.A.* **115**, 3225–3230 (2018). 10.1073/pnas.1721690115.
12. H. Hübener, U. De Giovannini, C. Schäfer, J. Andberger, M. Ruggenthaler, J. Faist, A. Rubio, Engineering quantum materials with chiral optical cavities. *Nat. Mater.* **20**, 438–442 (2021). 10.1038/s41563-020-00801-7.
13. A. Lininger, G. Palermo, A. Guglielmelli, G. Nicoletta, M. Goel, M. Hinczewski, G. Strangi, Chirality in light–matter interaction. *Adv. Mater.*, 2107325 (2022). 10.1002/adma.202107325.
14. V. V. Tuchin, L. V. Wang, D. A. Zimnyakov, *Optical Polarization in Biomedical Applications*. (Springer, 2006).
15. D.-Y. Kim, Potential application of spintronic light-emitting diode to binocular vision for three-dimensional display technology. *J. Korean Phys. Soc.* **49**, S505–S508 (2006).
16. C. D. Stanciu, F. Hansteen, A. V. Kimel, A. Kirilyuk, A. Tsukamoto, A. Itoh, T. Rasing, All-optical magnetic recording with circularly polarized light. *Phys. Rev. Lett.* **99**, 047601 (2007). 10.1103/PhysRevLett.99.047601.
17. R. Farshchi, M. Ramsteiner, J. Herfort, A. Tahraoui, H. T. Grahn, Optical communication of spin information between light emitting diodes. *Appl. Phys. Lett.* **98**, 162508 (2011). 10.1063/1.3582917.

18. Y. Yang, R. C. da Costa, M. J. Fuchter, A. J. Campbell, Circularly polarized light detection by a chiral organic semiconductor transistor. *Nat. Photonics* **7**, 634–638 (2013). 10.1038/nphoton.2013.176.
19. S. H. Lee, S.-H. Lee, S.-U. Kim, S. Kang, S.-D. Lee, Concept of chiral image storage and selection based on liquid crystals by circular polarization. *Opt. Express* **27**, 11661–11672 (2019). 10.1364/OE.27.011661.
20. Y. Shirasaki, G. J. Supran, M. G. Bawendi, V. Bulović, Emergence of colloidal quantum-dot light-emitting technologies. *Nat. Photonics* **7**, 13–23 (2013). 10.1038/nphoton.2012.328.
21. F. Fries, M. Fröbel, P. Y. Ang, S. Lenk, S. Reineke, Real-time beam shaping without additional optical elements. *Light Sci. Appl.* **7**, 18 (2018). 10.1038/s41377-018-0014-0.
22. X. Fu, Y. Mehta, Y.-A. Chen, L. Lei, L. Zhu, N. Barange, Q. Dong, S. Yin, J. Mendes, S. He, R. Gogusetti, C.-H. Chang, F. So, Directional polarized light emission from thin-film light-emitting diodes. *Adv. Mater.* **33**, 2006801 (2021). 10.1002/adma.202006801.
23. B. R. Sutherland, E. H. Sargent, Perovskite photonic sources. *Nat. Photonics* **10**, 295–302 (2016). 10.1038/nphoton.2016.62.
24. S. A. Veldhuis, P. P. Boix, N. Yantara, M. Li, T. C. Sum, N. Mathews, S. G. Mhaisalkar, Perovskite materials for light-emitting diodes and lasers. *Adv. Mater.* **28**, 6804–6834 (2016). 10.1002/adma.201600669.
25. M. D. Smith, B. A. Connor, H. I. Karunadasa, Tuning the luminescence of layered halide perovskites. *Chem. Rev.* **119**, 3104–3139 (2019). 10.1021/acs.chemrev.8b00477.
26. X.-K. Liu, W. Xu, S. Bai, Y. Jin, J. Wang, R. H. Friend, F. Gao, Metal halide perovskites for light-emitting diodes. *Nat. Mater.* **20**, 10–21 (2021). 10.1038/s41563-020-0784-7.
27. G. Long, R. Sabatini, M. I. Saidaminov, G. Lakhwani, A. Rasmita, X. Liu, E. H. Sargent, W. Gao, Chiral-perovskite optoelectronics. *Nat. Rev. Mater.* **5**, 423–439 (2020). 10.1038/s41578-020-0181-5.
28. G. Long, C. Jiang, R. Sabatini, Z. Yang, M. Wei, L. N. Quan, Q. Liang, A. Rasmita, M. Askerka, G. Walters, X. Gong, J. Xing, X. Wen, R. Quintero-Bermudez, H. Yuan, G. Xing, X. R. Wang, D. Song, O. Voznyy, M. Zhang, S. Hoogland, W. Gao, Q. Xiong, E. H. Sargent, Spin control in reduced-dimensional chiral perovskites. *Nat. Photonics* **12**, 528–533 (2018). 10.1038/s41566-018-0220-6.
29. J. Ma, H. Wang, D. Li, Recent progress of chiral perovskites: Materials, synthesis, and properties. *Adv. Mater.* **33**, 2008785 (2021). 10.1002/adma.202008785.
30. I. C. Seo, Y. Lim, S.-C. An, B. H. Woo, S. Kim, J. G. Son, S. Yoo, Q. H. Park, J. Y. Kim, Y. C. Jun, Circularly polarized emission from organic–inorganic hybrid perovskites *via* chiral fano resonances. *ACS Nano* **15**, 13781–13793 (2021). 10.1021/acsnano.1c05421.
31. J. Tian, G. Adamo, H. Liu, M. Klein, S. Han, H. Liu, C. Soci, Optical rashba effect in a light-emitting perovskite metasurface. *Adv. Mater.* **34**, 2109157 (2022). 10.1002/adma.202109157.
32. S. Kim, B. H. Woo, S.-C. An, Y. Lim, I. C. Seo, D.-S. Kim, S. Yoo, Q. H. Park, Y. C. Jun, Topological control of 2D perovskite emission in the strong coupling regime. *Nano Lett.* **21**, 10076–10085 (2021). 10.1021/acs.nanolett.1c03853.
33. Y. Lim, I. C. Seo, S.-C. An, Y. Kim, C. Park, B. H. Woo, S. Kim, H.-R. Park, Y. C. Jun, Maximally chiral emission via chiral quasibound states in the continuum. *Laser Photonics Rev.* **17**, 2200611 (2023). 10.1002/lpor.202200611.
34. C.-T. Wang, K. Chen, P. Xu, F. Yeung, H.-S. Kwok, G. Li, Fully chiral light emission from $CsPbX_3$ perovskite nanocrystals enabled by cholesteric superstructure stacks. *Adv. Funct. Mater.* **29**, 1903155 (2019). 10.1002/adfm.201903155.
35. S. Liu, X. Liu, Y. Wu, D. Zhang, Y. Wu, H. Tian, Z. Zheng, W.-H. Zhu, Circularly polarized perovskite luminescence with dissymmetry factor up to 1.9 by soft helix bilayer device. *Matter* **5**, 2319–2333 (2022). 10.1016/j.matt.2022.05.012.
36. Y. Deng, M. Wang, Y. Zhuang, S. Liu, W. Huang, Q. Zhao, Circularly polarized luminescence from organic micro−/nano-structures. *Light Sci. Appl.* **10**, 76 (2021). 10.1038/s41377-021-00516-7.
37. J. Jia, X. Cao, X. Ma, J. De, J. Yao, S. Schumacher, Q. Liao, H. Fu, Circularly polarized electroluminescence from a single-crystal organic microcavity light-emitting diode based on photonic spin-orbit interactions. *Nat. Commun.* **14**, 31 (2023). 10.1038/s41467-022-35745-w.
38. Y.-H. Kim, Y. Zhai, H. Lu, X. Pan, C. Xiao, E. A. Gaulding, S. P. Harvey, J. J. Berry, Z. V. Vardeny, J. M. Luther, M. C. Beard, Chiral-induced spin selectivity enables a room-temperature spin light-emitting diode. *Science* **371**, 1129–1133 (2021). 10.1126/science.abf5291.
39. C. Ye, J. Jiang, S. Zou, W. Mi, Y. Xiao, Core–shell three-dimensional perovskite nanocrystals with chiral-induced spin selectivity for room-temperature spin light-emitting diodes. *J. Am. Chem. Soc.* **144**, 9707–9714 (2022). 10.1021/jacs.2c01214.
40. J. Wang, C. Zhang, H. Liu, R. McLaughlin, Y. Zhai, S. R. Vardeny, X. Liu, S. McGill, D. Semenov, H. Guo, R. Tsuchikawa, V. V. Deshpande, D. Sun, Z. V. Vardeny, Spin-optoelectronic devices based on hybrid organic-inorganic trihalide perovskites. *Nat. Commun.* **10**, 129 (2019). 10.1038/s41467-018-07952-x.
41. M. V. Gorkunov, A. A. Antonov, Y. S. Kivshar, Metasurfaces with maximum chirality empowered by bound states in the continuum. *Phys. Rev. Lett.* **125**, 093903 (2020). 10.1103/PhysRevLett.125.093903.
42. M. V. Gorkunov, A. A. Antonov, V. R. Tuz, A. S. Kupriianov, Y. S. Kivshar, Bound states in the continuum underpin near-lossless maximum chirality in dielectric metasurfaces. *Adv. Opt. Mater.* **9**, 2100797 (2021). 10.1002/adom.202100797.
43. J. Wu, X. Xu, X. Su, S. Zhao, C. Wu, Y. Sun, Y. Li, F. Wu, Z. Guo, H. Jiang, H. Chen, Observation of giant extrinsic chirality empowered by quasi-bound states in the continuum. *Phys. Rev. Appl.* **16**, 064018 (2021). 10.1103/PhysRevApplied.16.064018.
44. E. Plum, N. I. Zheludev, Chiral mirrors. *Appl. Phys. Lett.* **106**, 221901 (2015). 10.1063/1.4921969.
45. J. Feis, D. Beutel, J. Köpfler, X. Garcia-Santiago, C. Rockstuhl, M. Wegener, I. Fernandez-Corbaton, Helicity-preserving optical cavity modes for enhanced sensing of chiral molecules. *Phys. Rev. Lett.* **124**, 033201 (2020). 10.1103/PhysRevLett.124.033201.
46. K. Voronin, A. S. Taradin, M. V. Gorkunov, D. G. Baranov, Single-handedness chiral optical cavities. *ACS Photonics* **9**, 2652–2659 (2022). 10.1021/acsphotonics.2c00134.
47. A. V. Kondratov, M. V. Gorkunov, A. N. Darinskii, R. V. Gainutdinov, O. Y. Rogov, A. A. Ezhov, V. V. Artemov, Extreme optical chirality of plasmonic nanohole arrays due to chiral Fano resonance. *Phys. Rev. B* **93**, 195418 (2016). 10.1103/physrevb.93.195418.
48. E. D. Palik, *Handbook of Optical Constants of Solids* (Academic Press, 1998).
49. H. Wang, X. Zhang, Q. Wu, F. Cao, D. Yang, Y. Shang, Z. Ning, W. Zhang, W. Zheng, Y. Yan, S. V. Kershaw, L. Zhang, A. L. Rogach, X. Yang, Trifluoroacetate induced small-grained $CsPbBr_3$ perovskite films result in efficient and stable light-emitting devices. *Nat. Commun.* **10**, 665 (2019). 10.1038/s41467-019-08425-5.
50. Y. J. Yoon, Y. S. Shin, H. Jang, J. G. Son, J. W. Kim, C. B. Park, D. Yuk, J. Seo, G.-H. Kim, J. Y. Kim, Highly stable bulk perovskite for blue LEDs with anion-exchange method. *Nano Lett.* **21**, 3473–3479 (2021). 10.1021/acs.nanolett.1c00124.
51. L. D. Landau, E. M. Lifshitz, *Electrodynamics of Continuous Media* (Pergamon Press, 1984).
52. A. A. Maksimov, I. I. Tartakovskii, E. V. Filatov, S. V. Lobanov, N. A. Gippius, S. G. Tikhodeev, C. Schneider, M. Kamp, S. Maier, S. Höfling, V. D. Kulakovskii, Circularly polarized light emission from chiral spatially-structured planar semiconductor microcavities. *Phys. Rev. B* **89**, 045316 (2014). 10.1103/PhysRevB.89.045316.
53. A. Vaskin, R. Kolkowski, A. F. Koenderink, I. Staude, Light-emitting metasurfaces. *Nanophotonics* **8**, 1151–1198 (2019). 10.1515/nanoph-2019-0110.
54. J. P. Hugonin, P. Lalanne, RETICOLO software for grating analysis. https://arxiv.org/abs/2101.00901 (2021).
55. Y. H. Ko, R. Magnusson, Wideband dielectric metamaterial reflectors: Mie scattering or leaky Bloch mode resonance? *Optica* **5**, 289 (2018). 10.1364/OPTICA.5.000289.
56. A. Overvig, A. Alù, Diffractive nonlocal metasurfaces. *Laser Photonics Rev.* **16**, 2100633 (2022). 10.1002/lpor.202100633.
57. Z. Wang, B. Zhang, H. Deng, Dispersion engineering for vertical microcavities using subwavelength gratings. *Phys. Rev. Lett.* **114**, 073601 (2015). 10.1103/PhysRevLett.114.073601.
58. B. E. A. Saleh, M. C. Teich, *Fundamentals of Photonics* (John Wiley & Sons, ed. 2, 2007), p. 257.

Acknowledgments: Y.C.J. thanks Q.-H. Park for helpful discussions. **Funding:** Y.C.J. was financially supported by the National Research Foundation (NRF) of Korea (NRF-2023R1A2C1004674 and NRF-2022R1F1A1074532) and Research Fund of the Ulsan National Institute of Science and Technology (1.230013.01 and 1.230017.01). Y.S.K. acknowledges a support of the Australian Research Council (grant no. DP210101292). Theoretical work of A.A.A. and M.V.G. was supported by the Russian Science Foundation (project 23-42-00091, https://rscf.ru/project/23-42-00091/). **Author contributions:** Y.C.J., J.Y.K., M.V.G., and Y.S.K. proposed the project. S.K., Y.K. and Y.S.S. fabricated and characterized devices. S.K., I.C.S., B.H.W., and Y.L. conducted measurements. Y.C.J., S.K., and S.-C.A. conducted analyses based on numerical simulations. M.V.G., A.A.A., and Y.S.K. conducted the CMT analysis and eigenmode simulation. All authors discussed the results and contributed to the manuscript preparation. **Competing interests:** The authors declare that they have no competing interest. **Data and materials availability:** All data needed to evaluate the conclusions in the paper are present in the paper and/or the Supplementary Materials.

Submitted 7 February 2023
Accepted 22 May 2023
Published 28 June 2023
10.1126/sciadv.adh0414